

## Quantifying magmatic volatiles by Raman microtomography of glass inclusion-hosted bubbles

F. Schiavi, N. Bolfan-Casanova, R. Buso, M. Laumonier, D. Laporte, K. Medjoubi, S. Venugopal, A. Gómez-Ulla, N. Cluzel, M. Hardiagon

### Supplementary Information

The Supplementary Information includes:

- Methods
- Tables S-1 and S-2
- Figures S-1 to S-5
- Supplementary Information References

### Methods

#### Raman spectrometry

Raman analysis of bubbles was carried out in back-scattered geometry using a Renishaw InVia confocal micro-spectrometer equipped with a  $532.1 \pm 0.3$  nm diode laser, a Peltier-cooled CCD detector of 1040 x 256 pixels, a Rayleigh rejection edge filter, a motorised XYZ stage and a Leica DM 2500M optical microscope. Daily calibration of the spectrometer was performed using a silicon standard ( $520.5 \text{ cm}^{-1}$  peak). We used a grating of 2400 grooves/mm, a 20- $\mu\text{m}$  slit aperture (high confocality setting), a  $\times 100$  microscope objective (numerical aperture = 0.9), and 1-8 mW laser power on the sample. These analytical conditions result in a spectral resolution of  $\sim 0.4 \text{ cm}^{-1}$  and in lateral and vertical spatial resolutions, respectively,  $\geq 0.3 \mu\text{m}$  and  $\sim 2 \mu\text{m}$  near the sample surface. The WIRE™ 4.3 to 4.4 software recorded the spectra in the  $\sim 200$ -1400 and 2900-3800  $\text{cm}^{-1}$  wavenumber ranges, which contain the main vibrational modes of the glass, mineral and fluid phases and the O-H stretching region.

Raman tomographic measurements allow to extract chemical information non-destructively from the interior of samples with high spatial and spectral resolution (Yesiltas *et al.*, 2018). Raman tomography was performed on bubbles having



diameters of 8 to 44  $\mu\text{m}$  and located at a maximum depth of 40  $\mu\text{m}$  from the olivine surface. The best results were obtained when bubbles were  $< 20 \mu\text{m}$  deep. Acquisitions were collected with a sampling step distance of 0.3-2  $\mu\text{m}$  in the horizontal ( $X$ - $Y$ ) plane and 1-2  $\mu\text{m}$  along the vertical  $Z$ -axis, depending on the bubble size. For each bubble, 3D mapping produced a single hypermap of many tens of thousands of spectra in the  $X$ - $Y$ - $Z$  space. Acquisition time was  $\geq 10$  s/point, which resulted, on average, in a three-day analytical session time for a single tomography. For instance, mapping a bubble of 10  $\mu\text{m}$  in diameter with a 0.5- $\mu\text{m}$  sampling step and acquisition time of 15 s/point takes about 3 days. Significantly longer times ( $\geq 1$  week) would be required for larger bubbles ( $\geq 20 \mu\text{m}$  in diameter). The WIRE™ software was used to collect, process, and view 3D volume data, allowing spectral information to be analysed in all dimensions simultaneously.

Signal intensity of a given material depends on its Raman scattering efficiency, density, absorptivity, and lattice orientation in anisotropic crystals (*e.g.*, Haskin *et al.*, 1997). Therefore, the post-analysis data processing needed to reconstruct the volume of a bubble requires an accurate examination of the entire set of acquired spectra. Although some processing steps can be performed automatically on the entire data set, this task usually takes several hours or even few days in the case of complex bubbles containing many mineral phases. Data processing consists of several steps. 1) Narrow random peaks known as cosmic rays are identified and removed from the datasets. 2) The baseline is subtracted from the spectra by fitting the most appropriate polynomial function passing through anchor points in peak-free spectral regions. 3) A spectrum can be simple, enclosing the peaks of a single phase, or it can represent a complex mixture of signals coming from two or three different phases. Therefore, for each phase present inside the bubble, a representative, well distinct peak must be selected, generally corresponding to the strongest vibrational mode. 4) For each phase, a 3D distribution map of the peak intensity is created using the ‘signal to baseline’ parameter to calculate the area under the selected peak. 5) The volume where a phase is present is defined by setting a threshold of intensity of the selected peak. The core of a mineral produces an intense peak, whereas the intensity of the signal decreases quite rapidly at its rim, on both horizontal and vertical planes. Consequently, the volume of a phase can be delimited by carefully analysing the lateral and vertical variations in peak intensity. A complication derives from the fact that the intensity of Raman signals decreases when deepening into the sample. This requires analysing several horizontal ( $X$ - $Y$ ) slices along  $Z$  and slightly adjusting the threshold set for each phase on each slice. 6) Volume reconstruction of the bubble is achieved by merging the 3D maps of all phases into a combined 3D representation on which different phases are identified by different colours.

The software ImageJ was used to estimate the area fractions of each mineral and fluid phases in all  $X$ - $Y$  sections to quantify the volumes occupied by each phase in the bubble. The diameter of the bubble defined by the Raman tomography was checked against the diameter measured with an optical microscope. If the analysed bubble had an approximately spherical shape, the volumes between two adjacent  $X$ - $Y$  sections (spherical segments) were calculated based on geometric models and trigonometric functions using the radius of each section and the distances between adjacent sections. For the top and bottom  $X$ - $Y$  sections, the volume was calculated using the equation for a spherical cap. To estimate the volumetric fraction ( $\varphi$ ) of a phase in the bubble, the area fraction of that phase in each section was multiplied by the relative volume (vol %) of the associated spherical segment or spherical cap, and then these fractions were summed over all spherical segments and caps. Finally, the recovered volume fractions of mineral phases were converted to mass or concentration values using the appropriate densities. For the fluid phase, the density of  $\text{CO}_2$  derived from the distance between the Fermi diad ( $\Delta$ ,  $\text{cm}^{-1}$ ; Wang *et al.*, 2011) was multiplied by the volume to obtain the mass of  $\text{CO}_2$ . The total  $\text{CO}_2$  mass in the bubble was obtained by adding the mass of fluid  $\text{CO}_2$  and the mass of  $\text{CO}_2$  stored in mineral phases such as carbonates. The total S mass in the bubble was obtained by adding the mass of S stored in sulfates and sulfides.

The procedure described above includes several sources of error affecting the volume reconstruction and estimation, and so the quantification of volatile species in the inclusion.

*Uncertainties associated with sample features and sample preparation.* In general, volume approximations are less accurate in the case of inclusions or bubbles with irregular shapes. In this case, X-ray microtomography can be used to



accurately determine the volume of inclusions and bubbles. This allows avoiding unprecise assumptions about the shape of the inclusion and the length of the third dimension (*i.e.* inclusion thickness; see Tucker *et al.*, 2019, for discussion about this issue). The accuracy of Raman microtomography is sensitive to features intrinsic to the sample: for instance, the technique works better when there is a small number of large crystals on the bubble walls than in the case of a coating of tiny crystals of different mineral phases. In any case, a good practice to increase the quality of Raman spectra is to bring the bubble at approximately 5  $\mu\text{m}$  from the surface of the host crystal by careful polishing: the shallower the bubble, the better the confocality and the signal intensity.

*Uncertainties associated with data acquisition.* A major parameter in Raman microtomography is the size of the sampling step. The error may be reduced by using a shorter sampling step, but this is at the cost of a longer acquisition time. Steps smaller than the size of minerals allow a better determination of the mineral volume. Nonetheless, the vertical spatial resolution of the technique is generally larger than the average size of mineral phases, resulting in a major source of error. Moreover, while isolated crystals can be defined quite easily, crystal aggregates are imaged as large continuous masses. This can result into overestimation of the mineral volume if empty spaces between crystals cannot be detected. In the most complex scenario, crystals of different sizes and/or compositions grow close to each other, which may result in overlooking of the smallest crystals ( $\ll 1 \mu\text{m}$ ) or of the less efficiently scattering mineral. This concerns especially the deeper half of the bubble because the absolute Raman signal decreases with depth.

*Uncertainties associated with data treatment: subtraction of spectral baseline, setting of intensity thresholds, 3D volume reconstruction.* The error associated with baseline fitting for the entire dataset remains low if care is taken to accurately check the resulting baselined spectra. The effect of the intensity threshold may be more important. In order to evaluate the sensitivity of 3D volume reconstruction to the intensity threshold, several 2D maps of a given *X-Y* section were generated by varying the threshold setting (*i.e.* by shifting phase boundaries) to obtain an upper (maximum) and a lower (minimum) limit for the volume of the mineral phases. Examining how the volume of each phase changes with varying the detection threshold is a good practice for estimating the error associated with the volumetric reconstruction. This procedure yielded uncertainties in the estimated mass of volatile components generally lower than 30 % relative. In general, the signal intensity of the host phases (*i.e.* olivine and glass) drops rapidly inside the bubble, which helps reconstruct the bubble volume. However, in the case of large bubbles, the threshold must be adjusted along the vertical axis because of the attenuation of signal intensity with depth (Everall, 2010).

*Uncertainties associated with the conversion of volume to mass.* The densities of fluid and mineral phases are required to convert volumes to masses. The estimate of  $\text{CO}_2$  density from the distance between the Fermi diad depends on which densimeter is used; the densimeter by Wang *et al.* (2011) is associated to an error of  $\pm 0.025 \text{ g/cm}^3$ . The reader is referred to Lamadrid *et al.* (2017) for further information on this issue and associated errors. In the case of a mixed vapour phase (*e.g.*,  $\text{CO}_2$  and  $\text{SO}_2$ ; Venugopal *et al.*, 2020), the volumetric proportions of the components can be estimated by normalising peak intensities to the scattering efficiencies of those components (*e.g.*, Burke, 2001) assuming that the overall spectrometer response is constant in the frequency range of the measured spectrum. Uncertainties associated with density estimates for mineral phases are relatively small in the pressure range applicable to the studied glass inclusions and are not expected to significantly affect the quantification of volatile components. Another difficulty arises from the fact that mineral phases in the studied systems are sometimes solid solutions rather than pure endmembers, and that their compositions are not precisely known. In this case, the uncertainty on the exact composition of the solid solution will mainly impact the estimation of the mass of cations (*e.g.*, Ca, Mg, or Fe in carbonates) and secondarily that of the volatile components (*i.e.* C and S). Taken into account the uncertainties in the density of carbonate solid solutions (Table S-2), the standard deviation in the total  $\text{CO}_2$  content inside the bubble is  $< 15 \%$  relative. Last generation energy-dispersive X-ray spectroscopy (EDS) detectors allow to work efficiently at low electron accelerating voltage and to reach spatial resolution of EDS analysis of the order of 50-100 nm at 5 kV. With such a spatial resolution, it will be possible to determine the composition of minerals inside bubbles, which are typically a few hundred nm long (Fig. 1b), thus reducing the uncertainty associated with mineral density.



The advantage of Raman microtomography is that it allows us for the identification and the volume quantification of the phases present in a glass inclusion-hosted bubble with good precision, undestructively, fairly quickly and at a modest cost. A further advantage of Raman microtomography is that the required sample preparation is relatively simple and rapid. The prospects for improvement relate mainly to the automation of spectrum processing for systematic localisation of interfaces. The main limitation is linked to the size of the condensate crystals that is often less than or equal to the spatial resolution of the technique. This difficulty can be resolved by combining Raman microtomography to another technique such as synchrotron-based XRF mapping and 3D microtomography or focused ion beam-scanning electron microscopy, which have better spatial resolution but are heavier to implement and much more expensive. The combination of multiple techniques provides access to a complete inventory of the phases involved in glass-hosted bubbles, to their volumes and to a range of microtextural parameters (crystal size distribution and shape).

### Synchrotron X-ray microtomography and 2D XRF mapping

Synchrotron experiments were performed by using the scanning X-ray nanoprobe end station at the NANOSCOPIUM beamline (SOLEIL) (Medjoubi *et al.*, 2013; Somogyi *et al.*, 2015). Before the experiments, the olivine crystals were embedded in Crystalbond™ and polished on six sides in order to remove the surrounding matrix glass, to reduce crystal size to less than 700 µm (thickness was generally < 250 µm) and to minimise the depth of the bubble. In order to reduce the absorption by the matrix of the X-ray fluorescence emitted from the main probed elements and so obtain a significant signal, bubbles needed to be less than 10 µm deep inside the olivine. Each olivine sample was glued on an aluminum or brass cylinder and the cylinder was fixed on an aluminum holder.

Prior to the X-ray fluorescence (XRF) 2D scans, fast full field X-ray microtomography (voxel size of 0.65 µm<sup>3</sup>) was performed on the single crystals at a beam energy of 14 keV. This imaging modality provided information on the position, depth, shape and size of glass inclusions and bubbles, and the possible presence of fractures.

Whether for X-ray microtomography and 2D XRF mapping, the acquisition was done in a continuous mode (continuous movement of the rotation and linear translation stages) by using the FLYSCAN architecture which has been developed at SOLEIL (Medjoubi *et al.*, 2013) for fast multi-technique scanning X-ray imaging.

2D XRF mapping of inclusion-hosted bubbles was performed using a beam energy of 14 keV. The selected flat surface of the olivine crystal was positioned perpendicularly to the incoming parallel beam. As the primary monochromatic beam penetrated below the surface of the samples, the measurement provided a depth-integrated signal. Spatial elemental distribution was obtained from the analysis of the X-ray fluorescence spectrum measured in each pixel of the scan. For each element of interest, we preselected a spectral region of the full XRF spectrum whose area was then used to reconstruct the elemental distribution map (Medjoubi *et al.*, 2013; Somogyi *et al.*, 2015).

As a first step, moderate resolution (1 µm × 1 µm) 2D maps were rapidly collected with a low (typically 20 ms) integration time on an 80 µm × 80 µm area, comprising the bubble-bearing inclusion and part of the olivine host. After zooming in on the bubble, high-resolution and high-sensitivity (150 nm pixel size and 300 ms integration time) scanning was performed and lasted several hours, depending on the size of the bubble (*i.e.* up to 6 hours for a bubble of 40-µm diameter). Elements like Cu, Fe, and Ca provided elemental distribution maps with a highly significant signal to noise ratio, while lighter elements like Mg and Na could not be detected in a such hard-X-ray nano-probe beamline. Maps of Ca and Fe often consisted of overlapping signals coming from the bubble, the surrounding glass, and the olivine host; on the contrary, Cu was mostly detected in bubbles, thus producing clear, uncontaminated maps. Approaching the bubble as much as possible to the surface (~2 µm) resulted in the elimination of contamination by the glass, but at the cost of increasing the risk of losing bubbles during polishing. Fully quantitative measurements were not possible because of the self-absorption by olivine host crystals. The self-absorption also causes a drastic reduction of the transmission of



fluorescence signals with depth. Therefore, the most suitable samples for XRF mapping are bubbles close to the surface and rich in the elements of interest.

### **FIB-FESEM: Focused Ion Beam and Field Emission Scanning Electron Microscopy**

Bubbles in glass inclusions are microscopic objects (typically 10  $\mu\text{m}$ ) and the microcrystals on their walls constitute fragile microstructures. It is not straightforward to expose such tiny features at the surface of a polished section using standard preparation techniques (cutting, grinding, polishing), and the microcrystals inside the bubbles may be damaged during the preparation. To image the interior of a glass inclusion-hosted bubble, we used a correlative microscopy approach combining an X-ray tomography microscope to precisely locate bubbles and glass inclusions inside an olivine crystal, and a FIB-FESEM to excavate the bubble of interest and to make high-resolution images of its interior (Fig. 1). This work was done at the Carl ZEISS Microscopy GmbH demonstration centre in Oberkochen, Germany.

An olivine from Lac-d'Issarlès volcano, Ardèche, France, was selected for this task. We ground one side of the crystal until the bubble of interest was less than 50  $\mu\text{m}$  underneath the surface (as checked by optical microscopy). The exact position of the bubble inside the olivine crystal was determined using a ZEISS Xradia 620 Versa X-ray tomography microscope. The full olivine crystal (1.2  $\times$  1.5 mm) was imaged with a 0.78  $\mu\text{m}$  pixel size, and a detailed tomography of the region of interest (the glass inclusion hosting the bubble) was acquired with a 0.40  $\mu\text{m}$  pixel size. Afterwards, the sample holder with the olivine crystal was transferred into a ZEISS CROSSBEAM 550 FIB-FESEM. The bubble, which was at a depth of  $\sim$  40  $\mu\text{m}$  below the olivine surface, was first relocated with a precision of a few  $\mu\text{m}$  by overlaying the SEM image with sections through the X-ray tomography. A gallium focused ion beam was used to progressively mill the olivine until the bubble was fully exposed. High-resolution secondary electron images of the bubble interior were acquired with in-lens detector at a voltage of 2 kV and a probe current of 800 pA.



## Supplementary Tables

**Table S-1** Average major element compositions (wt %) and standard deviations (second column) of glass inclusions from the studied samples

SAMPLE	ISS3-04		THU3		M8		LZ-TAO <sup>a</sup>		MMA <sup>b</sup>	
Location	Lac-d'Issarlès, Ardèche, France		Thueyts, Ardèche, France		Montcineyre, Puy-de-Dôme, France		Volcan de Tao, Lanzarote, Canary Islands, Spain		Mt Meager, GVB, British Columbia, Canada	
Geodynamic setting	Continental intraplate		Continental intraplate		Continental intraplate		Hotspot		Subduction zone	
Rock type	Basanitic tephra		Basanitic tephra		Basanitic tephra		Basanitic tephra		Basaltic breccia	
Oxides wt %										
SiO <sub>2</sub>	44.74	1.11	42.95	2.10	44.15	1.91	44.77	1.69	49.77	0.89
TiO <sub>2</sub>	2.66	0.14	2.76	0.26	3.36	0.54	3.33	0.27	1.40	0.10
Al <sub>2</sub> O <sub>3</sub>	15.48	0.84	14.97	1.00	15.71	0.39	15.20	0.87	17.43	0.44
FeO <sub>Tot</sub>	9.25	1.10	9.01	1.19	8.30	0.71	8.40	1.09	8.61	0.66
MnO	0.12	0.03	0.14	0.06	0.12	0.05	0.13	0.09	0.12	0.05
MgO	7.18	0.74	7.95	0.79	6.21	0.49	5.10	0.78	5.07	0.33
CaO	11.07	1.01	12.21	1.13	11.60	0.49	13.20	1.08	8.96	0.62
Na <sub>2</sub> O	4.10	0.23	4.18	0.32	3.98	0.06	3.83	0.73	3.82	0.32
K <sub>2</sub> O	1.50	0.28	1.73	0.18	1.86	0.34	1.47	0.20	0.77	0.04
P <sub>2</sub> O <sub>5</sub>	0.67	0.11	0.94	0.24	0.73	0.14	1.16	0.23	0.38	0.07
Total	96.77		96.83		96.03		96.60		96.32	

*Notes:*

<sup>a</sup> Compositions from Gómez-Ulla *et al.* (2018).

<sup>b</sup> Compositions from Venugopal *et al.* (2020). GVB stands for Garibaldi Volcanic Belt.



**Table S-2** Nature and volumetric proportions of mineral and fluid phases filling the glass inclusion-hosted bubbles imaged by Raman tomography (see the notes at the bottom of the table)

SAMPLE	ISS3-04-8	THU3-1-Gr8	M8-Gr3-fDMI1	LZ-TAO-MI1	LZ-TAO2-fAMI2	MMA-MI203
Location	Lac-d'Issarlès, France	Thueyts, France	Montcineyre, France	Volcan de Tao, Spain	Volcan de Tao, Spain	Mt Meager, Canada
Host phase	olivine	olivine	olivine	olivine	olivine	olivine
Magma composition	basanite	basanite	basanite	basanite	basanite	basalt
<b>GLASS INCLUSION</b>						
Major axis (µm)	34.0	72.9	27.4	33.3	40.0	125
Medium axis (µm) <sup>a</sup>	28.4	69.8	20.2	28.0	32.5	109
Minor axis (µm)	22.7	66.7	13.0	22.7	25.0	93
Volume (cm <sup>3</sup> )	1.15 E-08	1.78 E-07	3.77 E-09	1.11 E-08	1.70 E-08	6.63 E-07
<b>BUBBLE</b>						
Diameter (µm)	16	28	8	9	14	44
Volume (cm <sup>3</sup> )	2.14 E-09	1.15 E-08	2.68 E-10	3.82 E-10	1.56 E-09	4.31 E-08
Volume %	18.7	6.5	7.1	3.4	9.2	6.5
<b>MINERAL PHASES IN THE BUBBLE</b>						
<b>CARBONATE</b>		(Ca,Mg)CO <sub>3</sub>		(Ca,Mg)CO <sub>3</sub>	CaCO <sub>3</sub>	(Ca,Mg)CO <sub>3</sub>
Density (g/cm <sup>3</sup> )		2.71 - 2.94		2.71 - 2.94	2.71	2.71 - 2.94
φ		0.33 ± 0.09		0.26 ± 0.07	0.068 ± 0.020	0.068 ± 0.012
Volume (cm <sup>3</sup> )		3.79 E-09		9.92 E-11	1.06 E-10	2.93 E-09
Mass (g)		1.03–1.11 E-08		2.69-2.92 E-10	2.88 E-10	7.94-8.61 E-09
<b>CARBONATE</b>	(Ca,Mg,Fe)CO <sub>3</sub>		(Ca,Mg,Fe)CO <sub>3</sub>		(Ca,Mg,Fe)CO <sub>3</sub>	(Mg,Fe)CO <sub>3</sub>
Density (g/cm <sup>3</sup> )	2.71 – 3.96		2.71 – 3.96		2.71 – 3.96	2.94 – 3.96
φ	0.25 ± 0.05		0.28 ± 0.06		0.042 ± 0.006	0.025 ± 0.004
Volume (cm <sup>3</sup> )	5.36 E-10		7.61 E-11		6.50 E-11	1.08 E-09
Mass (g)	1.45-2.12 E-09		2.06-3.01 E-10		1.76-2.57 E-10	3.17-4.26 E-09
<b>CARBONATE</b>	NaHCO <sub>3</sub>		NaHCO <sub>3</sub>		NaHCO <sub>3</sub>	
Density (g/cm <sup>3</sup> )	2.21		2.21		2.21	
φ	0.033 ± 0.008		0.005 ± 0.001		0.028 ± 0.004	
Volume (cm <sup>3</sup> )	7.07 E-11		1.34 E-12		4.38 E-11	
Mass (g)	1.56 E-10		2.96 E-12		9.67 E-11	
<b>SULFIDE</b>	CuFeS <sub>2</sub>		CuFeS <sub>2</sub>	CuFeS <sub>2</sub>	CuFeS <sub>2</sub>	
Density (g/cm <sup>3</sup> )	4.2		4.2	4.2	4.2	
φ	0.008 ± 0.001		0.024 ± 0.008	0.030 ± 0.009	0.035 ± 0.012	
Volume (cm <sup>3</sup> )	1.71 E-11		6.46 E-12	1.14 E-11	5.41 E-11	
Mass (g)	7.20 E-11		2.71 E-11	4.81 E-11	2.27 E-10	
<b>SULFIDE</b>		FeS <sub>2</sub>	FeS <sub>2</sub>		CuS	FeS <sub>2</sub>
Density (g/cm <sup>3</sup> )		4.98	4.98		4.7	4.98
φ		0.007 ± 0.001	0.027 ± 0.011		0.014 ± 0.004	0.009 ± 0.002
Volume (cm <sup>3</sup> )		8.04 E-11	7.13 E-12		2.17 E-11	3.88 E-10
Mass (g)		4.00 E-10	3.55 E-11		1.02 E-10	1.93 E-09



Table S-2 cont.

SAMPLE	ISS3-04-8	THU3-1-Gr8	M8-Gr3- fDMI1	LZ-TAO-MI1	LZ-TAO2- fAMI2	MMA-MI203
MINERAL PHASES IN THE BUBBLE						
<b>SULFATE</b>					CaSO <sub>4</sub> / CaSO <sub>4</sub> ·2H <sub>2</sub> O	CaSO <sub>4</sub>
Density (g/cm <sup>3</sup> )					2.3 – 3.0	2.95
φ					0.043 ± 0.013	0.19 ± 0.04
Volume (cm <sup>3</sup> )					6.66 E-11	8.36 E-09
Mass (g)					1.55-1.96 E-10	2.47 E-08
<b>SULFATE</b>					K <sub>2</sub> Ca(SO <sub>4</sub> ) <sub>2</sub> ·H <sub>2</sub> O	CaSO <sub>4</sub> ·2H <sub>2</sub> O
Density (g/cm <sup>3</sup> )					2.58	2.33
φ					0.016 ± 0.004	0.012 ± 0.002
Volume (cm <sup>3</sup> )					2.45 E-11	5.17 E-10
Mass (g)					6.33 E-11	1.20 E-09
<b>SULFATE</b>						Na <sub>2</sub> SO <sub>4</sub>
Density (g/cm <sup>3</sup> )						2.68
φ						0.002 ± 0.0004
Volume (cm <sup>3</sup> )						8.62 E-11
Mass (g)						2.31 E-10
CUMULATIVE VOLUME FRACTIONS OF CARBONATES, SULFIDES and SULFATES						
φ carbonates	0.28 ± 0.06	0.33 ± 0.09	0.29 ± 0.06	0.26 ± 0.07	0.14 ± 0.03	0.09 ± 0.02
φ sulfides	0.008 ± 0.001	0.007 ± 0.001	0.05 ± 0.02	0.03 ± 0.01	0.05 ± 0.02	0.009 ± 0.002
φ sulfates					0.06 ± 0.02	0.21 ± 0.04
FLUID PHASES IN THE BUBBLE						
<b>CO<sub>2</sub></b>						
Distance Fermi diad (cm <sup>-1</sup> )	103.4	103.3	103.5	103.5	104.2	
Density (g/cm <sup>3</sup> ) <sup>b</sup>	0.26	0.23	0.33	0.33	0.63	
φ	0.71	0.66	0.66	0.71	0.76	
Volume (cm <sup>3</sup> )	1.52 E-09	7.62 E-09	1.77 E-10	2.71 E-10	1.18 E-09	
Mass (g)	3.95 E-10	1.75 E-09	5.85 E-11	8.94 E-11	7.44 E-10	
<b>H<sub>2</sub>O</b>	not detected	not detected	not detected	not detected	detected	detected
BUBBLE TOTAL CONTENT						
CO <sub>2</sub> mass (g) <sup>c</sup>	1.12-1.41 E-09	6.66-7.07 E-09	1.51-1.93 E-10	2.18-2.29 E-10	9.99 E-10 - 1.04 E-09	≥ 5.18 E-09
S mass (g) <sup>d</sup>	2.52 E-11	2.14 E-10	2.85 E-11	1.68 E-11	1.55-1.72 E-10	7.12 E-09
GLASS <sup>e</sup>						
Density (g/cm <sup>3</sup> )		2.8	2.8	2.8	2.8	2.75
Volume (cm <sup>3</sup> )		1.66 E-07	3.50 E-09	1.07 E-08	1.54 E-08	6.20 E-07
Mass (g)		4.65 E-07	9.79 E-09	2.99 E-08	4.32 E-08	1.71 E-06
CO <sub>2</sub> (ppm)		7896 <sup>f</sup>	7680 (955) <sup>f</sup>	2196 (1019) <sup>g</sup>	4500 <sup>f</sup>	1278 (220) <sup>h</sup>
S (ppm)		1850	2462 (596)	2608 <sup>g</sup>	2574 (579) <sup>g</sup>	2759 (451) <sup>h</sup>
H <sub>2</sub> O (wt%)		1.70	1.60 (0.24)	1.55 (0.21) <sup>g</sup>	1.26	2.55
CO <sub>2</sub> mass (g)		3.67 E-09	7.52 E-11	6.58 E-11	1.95 E-10	2.18 E-09
S mass (g)		8.61 E-10	2.41 E-11	7.81 E-11	1.11 E-10	4.70 E-09



Table S-2 cont.

SAMPLE	ISS3-04-8	THU3-1-Gr8	M8-Gr3- fDMI1	LZ-TAO-MI1	LZ-TAO2- fAMI2	MMA-MI203
PERCENTAGES OF VOLATILES SEQUESTERED IN THE BUBBLE						
<b>CO<sub>2</sub> %</b>						
- If bubble was entirely filled by CO <sub>2</sub>		42	54	66	83	
- Considering both minerals and fluids		64 – 66	67 – 72	77 – 78	84	70 – 73
<b>S %</b>						
in minerals		20	54	18	58 – 61	60
VOLATILES IN THE INCLUSIONS (glass + fluids + minerals)						
CO <sub>2</sub> (wt%)		2.08 – 2.16	2.15 – 2.54	0.91 – 0.95	2.51 – 2.58	≥ 0.40
S (ppm)		2162	4984	3060	5589-5953	6479

*Notes:*

$\phi$  is the volume fraction of the mineral or fluid phase in the bubble. As a whole, crystals occupy 24 to 34 % of bubble volumes; 27 vol% is equivalent to a mineral layer of 500 nm thickness at the rim of a 10- $\mu$ m-diameter bubble.

It was not possible to estimate the quantity of H<sub>2</sub>O in the fluid phase.

Mineral densities are for room temperature and pressure conditions from Deer *et al.* (2013). In the presence of solid solutions, a range of density values (minimum - maximum) is indicated.

Glass density is an approximate calculated value.

<sup>a</sup> It corresponds to the arithmetic mean of the major and minor axes.

<sup>b</sup> CO<sub>2</sub> density calculated using the equation by Wang *et al.* (2011).

<sup>c</sup> Total CO<sub>2</sub> mass from carbonates and fluid phase.

<sup>d</sup> Total S mass from sulfates and sulfides.

<sup>e</sup> In parentheses are the standard deviations associated with the average values of concentrations in glass inclusions from the same eruptions.

<sup>f</sup> CO<sub>2</sub> concentrations measured by Raman spectrometry.

<sup>g</sup> Concentrations measured by Gómez-Ulla *et al.* (2018), using ion and electron microprobes.

<sup>h</sup> Concentrations measured by Venugopal *et al.* (2020), using ion and electron microprobes.



## Supplementary Figures

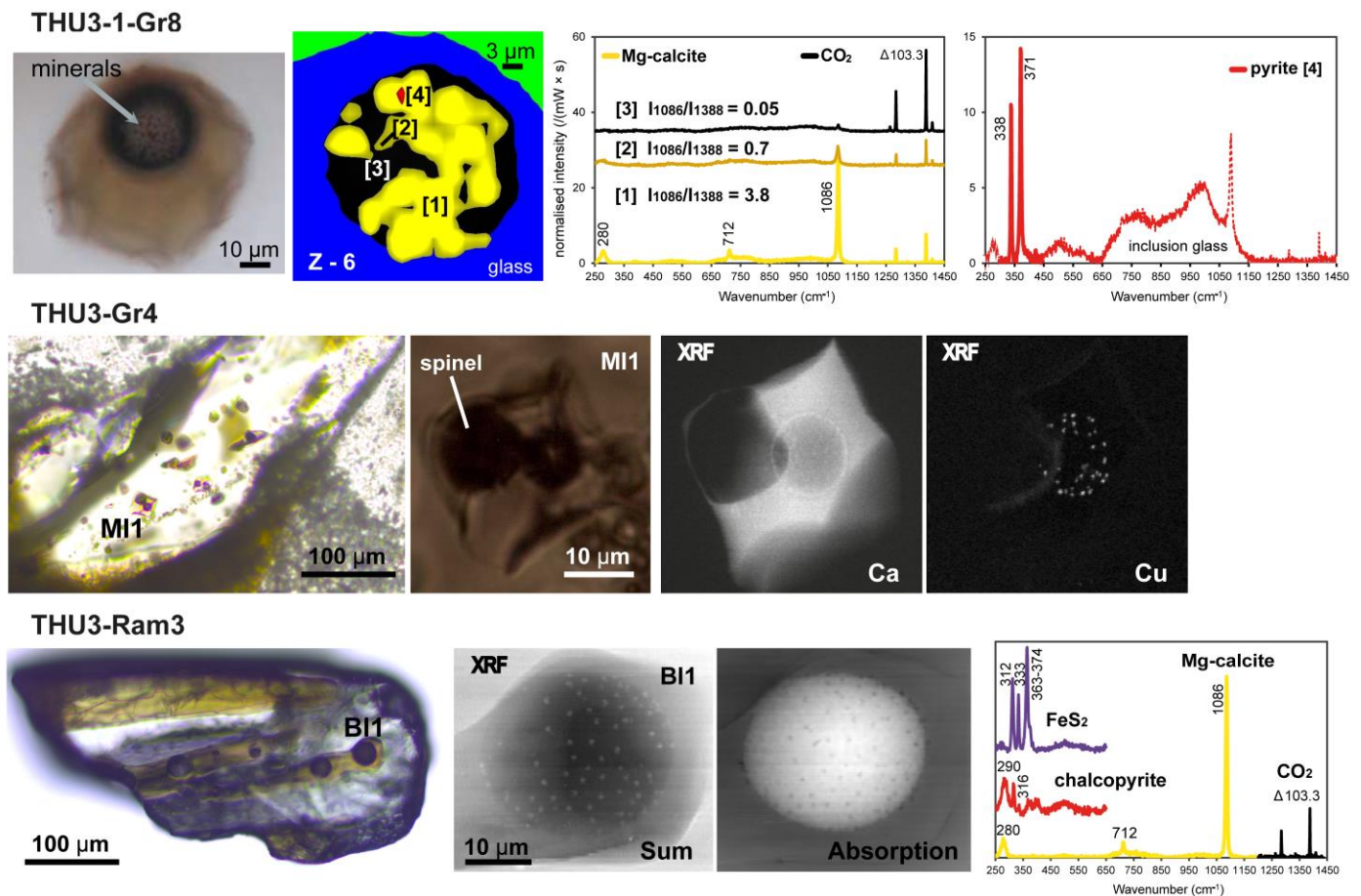


**Figure S-1** Glass inclusion-hosted bubbles in three olivine grains from Thueyts volcano (THU3-Gr8, THU3-Gr4 and THU3-Ram3). The inclusions/embayments are glassy and light brown in colour. Glass inclusions have variable morphologies from ovoid to faceted with olivine crystallised on the inclusion rim. Bubble diameters are  $< 30 \mu\text{m}$ . The ratio of bubble to inclusion volume ranges from  $\sim 0.05$  to  $0.1$ . **(Upper row)** Optical microscope image, 2D slice from the Raman map and associated spectra of sample THU3-Gr8 (same as in Fig. 2). Colour shadows in the 2D slice help delimiting different grains or aggregates of Mg-calcite. Numbers in brackets associate Raman spectra with acquisition points on the map. Raman spectra are mixture of signals from different phases, so for each phase the main peaks are indicated. The spectra are offset for clarity. Distance between the Fermi diad ( $\Delta$ ) is reported near the  $\text{CO}_2$  spectrum (also in the next figures). The intensity ratio of main peaks of Mg-calcite ( $1086 \text{ cm}^{-1}$ ) and  $\text{CO}_2$  ( $1388 \text{ cm}^{-1}$ ) decreases rapidly near the grain edges and in regions with reduced carbonate thickness (compare spectra [1] and [2]): this helps localising accurately the mineral/gas interface. On the y-axis, Raman intensity is normalised to laser power and acquisition time (also in next figures). **(Middle row)** Optical images of olivine THU3-Gr4 and glass inclusion MI1, and 2D X-ray fluorescence images (XRF) showing the elemental distributions maps of calcium and copper in the inclusion. The inclusion contains a magnetite crystal. The bubble is coated by Cu-bearing sulfide crystals and a carbonate layer that well defines the bubble rim. **(Lower row)** Optical image of the olivine THU3-Ram3 hosting glass embayments, synchrotron XRF and absorption maps of the bubble BI1, and Raman spectra of the phases present in the bubble. The minerals are evenly distributed on the bubble rim and display uniform size. The absorption image shows that the minerals partially project outward into the glass.

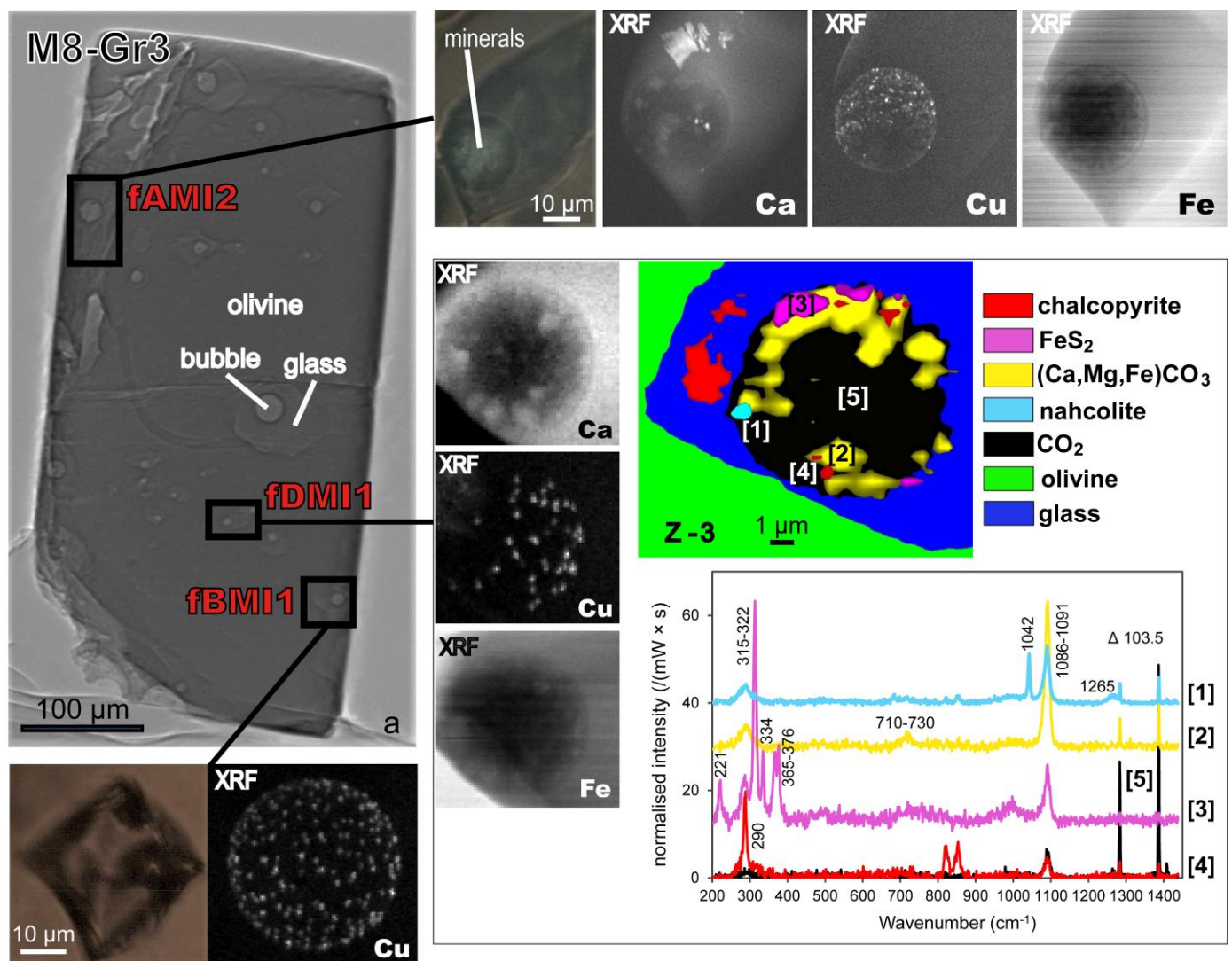


**Figure S-2** Olivine grain from Montcineyre volcano (M8-Gr3) imaged by synchrotron X-ray tomography (a). The olivine hosts several bubble-bearing glass inclusions, which are glassy and light to dark brown in colour. They have different shapes; the length of their major axis varies from  $\sim 10$  to  $80 \mu\text{m}$ . Bubble diameters are between  $\sim 8$  and  $30 \mu\text{m}$ . The ratio of bubble to inclusion volume ranges from  $\sim 0.05$  to  $0.1$ . The olivine was polished to bring three inclusion-hosted bubbles (fAMI2, fDMI1 and fBMI1) very close to an olivine facet and analyse them using 2D X-ray fluorescence. **fAMI2**: optical image of the inclusion and XRF maps of calcium, copper, and iron. Note that mineral phases are abundant, and crystals are characterised by different shapes and sizes. **fBMI1**: optical image of the inclusion and XRF map of copper in the bubble. A large number of small sulfide crystals coat the bubble rim. **fDMI1** (same as in Fig. 2): XRF maps of calcium, copper, and iron in the bubble, a 2D slice extracted from the Raman tomography and associated spectra of the phases filling the bubble. Numbers in brackets on the 2D slice indicate where the spectra were acquired. Raman spectra are mixture of signals from different phases, so for each phase the main peaks are indicated. The large peaks of carbonate indicate either the presence of carbonate solid solutions or simultaneous collection of signals from different grains. Both XRF and Raman tomography show diffuse presence of Cu-bearing sulfides in the glass nearby the bubble. Heavy elements, like copper, have the highest X-ray yields, thus providing the best XRF images. Copper was easily detected in all bubbles, while the presence of other elements was sometimes hidden by the stronger absorption from the olivine or the glass. Iron distribution maps are partially coupled with calcium or copper maps. Minerals inside the bubbles are generally ten-to-hundreds of nm in size, but Ca-bearing minerals can reach few  $\mu\text{m}$  size (fAMI2, fDMI1). Crystals can be uniformly (fBMI1) or unevenly (fAMI2, fDMI1) distributed, and their number density is highly variable.

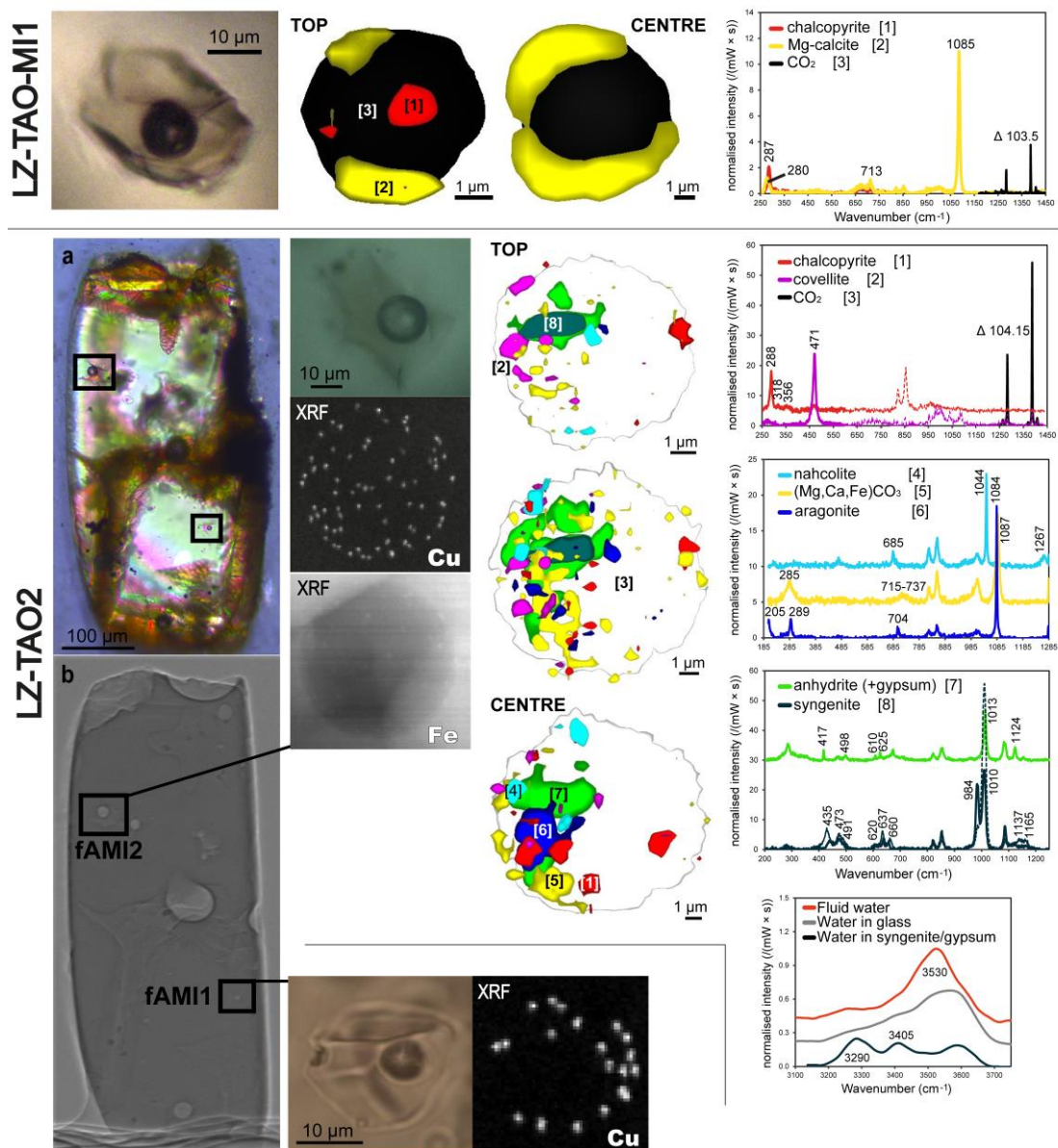


**Figure S-3** Glass inclusion-hosted bubbles in two olivine grains from Volcàn de Tao in Lanzarote. (**Upper row**) Bubble LZ-TAO-MI1 imaged by optical microscope and Raman tomography (same as in Fig. 3). Raman spectra of the phases filling the bubble and the associated acquisition points on the map are shown. (**Lower section**) Olivine LZ-TAO2 imaged by optical microscope (**a**) and synchrotron X-ray tomography (**b**). The olivine hosts several inclusions, which are glassy, light brown in colour, and with variable shape from ovoid to faceted. The length of their major axis varies from ~25 to 40  $\mu\text{m}$ . Some glass inclusions contain Cu-Fe sulfides. Bubble diameters are between 8 and 15  $\mu\text{m}$ . The ratio of bubble to inclusion volume ranges between ~0.03 and 0.1. Two bubbles (fAMI1 and fAMI2) were analysed using synchrotron XRF. **fAMI1**: optical image of the inclusion and XRF map of copper in the bubble showing unevenly distributed, equant-shaped sulfide crystals. **fAMI2** (same as in Fig. 3): optical image of the inclusion, XRF maps of copper and iron in the bubble, and 2D slices from Raman tomography representative of the upper half of the bubble (from top to centre). The mineral phases in the bubble are unevenly distributed. Raman spectra of  $\text{CO}_2$ , sulfides, carbonates, sulfates, and water are shown. Note the differences between spectra of water incorporated in the syngenite structure, fluid water in the bubble, and water dissolved in the surrounding glass. Numbers in brackets associate Raman spectra with acquisition points on the map. In both samples: although some grains seem to float in the gas in 2D, they are all connected to the bubble walls in 3D.

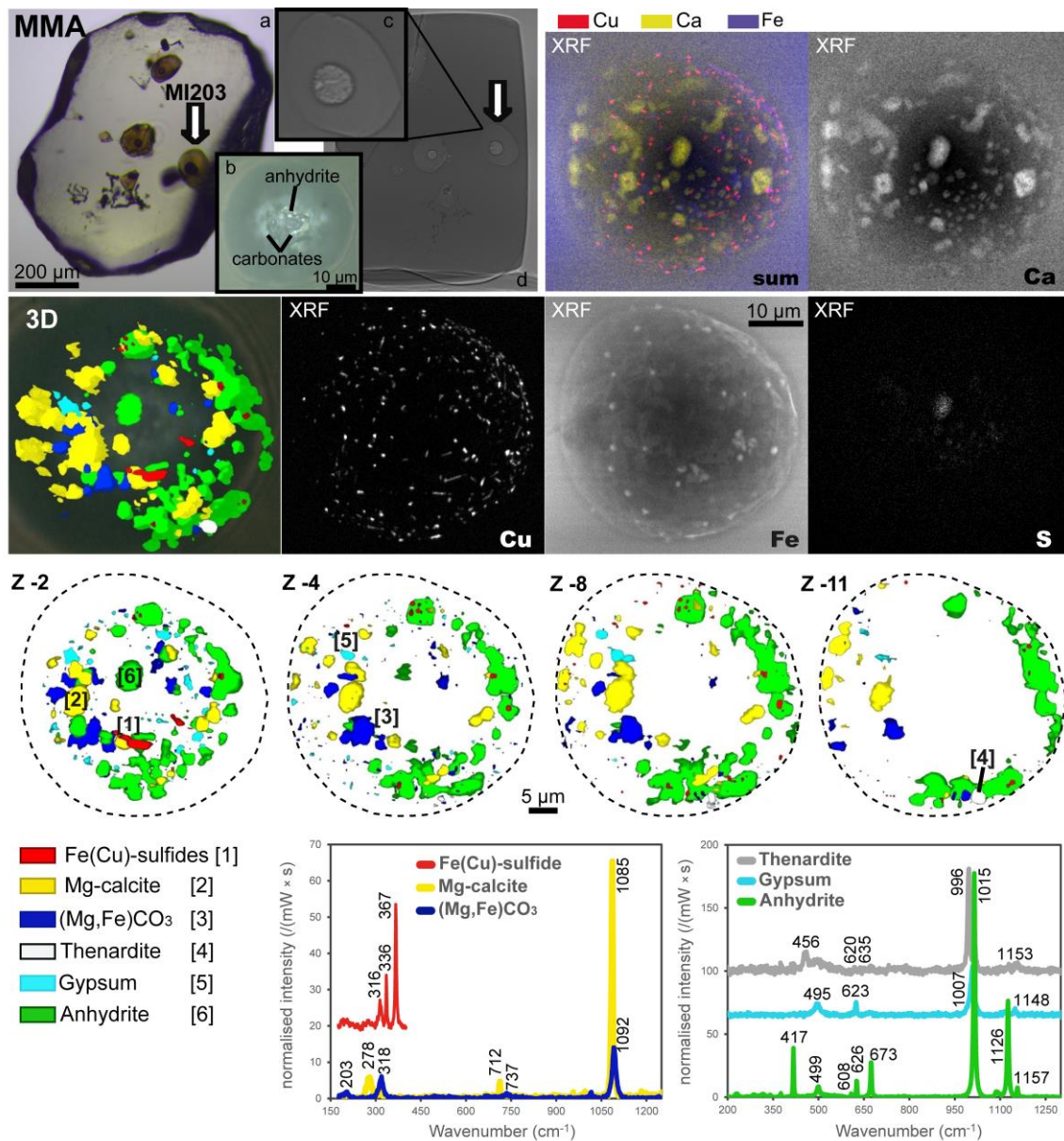


**Figure S-4** Glass inclusion-hosted bubble from Mount Meager (same as in Fig. 4) imaged by optical microscope (a, b), synchrotron X-ray tomography (c, d), 2D XRF maps of calcium, copper, iron, and sulfur, (3D) Raman tomography and 2D slices extracted from it. The inclusion is glassy, brown in colour and has an ovoid shape; bubble shape is not perfectly spherical. The sizes of the inclusion and bubble are reported in Table S-2. The rim of the bubble is well defined, especially on the Fe distribution map. A thin tube connecting the inclusion to the external melt likely explains the loss of CO<sub>2</sub> from the bubble. Abundant minerals, which are clearly visible in the images (b, c), partially fill the interior of the bubble. They are generally ten-to-hundreds of nm in size, but carbonates and sulfates reach few µm size. Ca-bearing phases show different polyhedral shapes, with tabular to rhombohedral habit. Iron map includes signals from Fe-bearing sulfides and carbonates. Calcium map includes contributions from Mg-calcite (with rhombohedral habit) and sulfates. Iron and copper XRF maps are partially coupled, implying that sulfides contain Cu in addition to Fe. Slight shifts of the Raman peaks of pyrite (or pyrrhotite) to lower wavenumbers, compared to expected values, are possibly due to increase in bond length caused by partial substitution of Fe by Cu. Cu-Fe sulfides form tiny lineaments. Numbers in brackets on the Raman maps indicate where the spectra were acquired. The two techniques provide coherent results relating to the spatial distribution of the elements and mineral phases detected: note the large isolated crystal of anhydrite (in the middle of the XRF sum and Raman maps), the large crystals of Mg-calcite (yellowish), small sulfide crystals (red), and anhedral Fe-bearing aggregates (blue). Also note the good match in crystal size between XRF and Raman maps (within 25% difference for the surface of the large anhydrite crystal). It can be observed that crystals/crystal aggregates tend to appear slightly wider in Raman maps than in XRF maps.

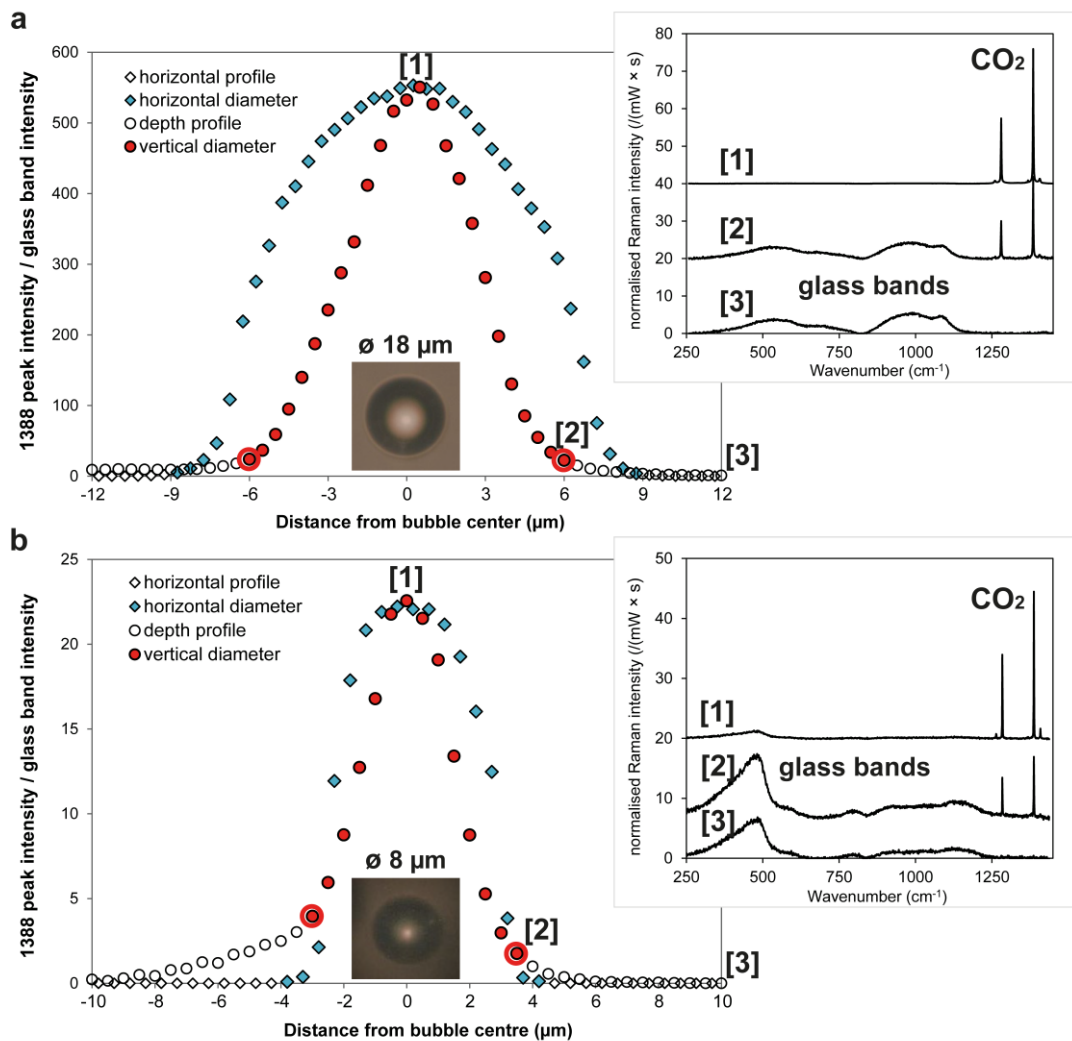


**Figure S-5** Intensity profiles of the CO<sub>2</sub> most intense peak (1388 cm<sup>-1</sup>) measured along the diameter of two bubbles in synthetic basaltic (a) and rhyolitic (b) glasses (Cluzel, 2007; Laporte *et al.*, 2016). Raman acquisitions were taken along two orthogonal directions passing through the centre of the bubble, with a 0.5 μm sampling step. Bubble diameters (∅) measured in the horizontal profiles match those measured on optical images. Bubble centre was at ~24 μm (a) and 19 μm (b) depth from the surface. For the vertical profile, the negative distance values indicate the radius below the bubble centre. In each point, the CO<sub>2</sub> peak intensity is normalised to the intensity of the glass band at ~1000 cm<sup>-1</sup> (a) or 480 cm<sup>-1</sup> (b). The coloured data points (blue in the horizontal profiles, red in the vertical ones) correspond to the points inside the glass bubbles. Along a horizontal axis, the CO<sub>2</sub> peak intensity varies from a maximum value at the bubble centre to a minimum value at the bubble/glass interface. The intensity of the glass band displays the opposite trend. Thus, the bubble/glass interface can be accurately localised in profiles of the intensity ratio CO<sub>2</sub>/glass. The intensity profiles along the vertical axis are shorter because of the mismatches of the refractive index ( $n$ ) at the air/glass ( $n_{\text{air}} = 1.0$  and  $n_{\text{glass}} \sim 1.5$ ) and glass/CO<sub>2</sub> interfaces ( $n_{\text{CO}_2} > 1.07$  at  $P \sim 8$  MPa; Besserer and Robinson, 1971). Due to lower in-depth spatial resolution, the intensity ratio drops to zero more slowly along the vertical axis (*i.e.* CO<sub>2</sub> peaks are still visible in the spectra collected outside the bubble volume), especially in the rhyolitic glass. Two inflection points (large red circles) define the size of the bubble on the vertical profile. When it is corrected for the effect of light refraction (real depth = measured depth  $\times n$ ), the distance between the inflection points is a good approximation of the bubble diameter and is equal to the horizontal diameter within 5 % and 20 % error, respectively, in basaltic and rhyolitic glasses. [1], [2] and [3] correspond to the spectra acquired, respectively, in the bubble centre, at the bubble/glass interface and in the glass. The associated uncertainty depends on the step size between two consecutive points and is  $\pm 0.5$  μm for 1 μm-step profiles.



## Supplementary Information References

- Besserer, G.J., Robinson, D.B. (1971) A high pressure autocollimating refractometer for determining coexisting liquid and vapor phase densities. *The Canadian Journal of Chemical Engineering* 49, 651-656.
- Burke, E.A.J. (2001) Raman microspectrometry of fluid inclusions. *Lithos* 55, 139-158.
- Cluzel, N. (2007) Simulation expérimentale de l'ascension et de la vésiculation des magmas rhyolitiques. Thèse en Sciences de la Terre, Université Blaise Pascal - Clermont-Ferrand II.
- Deer, W.A., Howie, R.A., Zussman, J. (2013) *An introduction to the rock-forming minerals*. Third edition, The Mineralogical Society, London.
- Everall, N.J. (2010) Confocal Raman microscopy: common errors and artefacts. *Analyt* 135, 2512-2522.
- Gómez-Ulla A. (2018) Historical eruptions of Lanzarote, Canary Islands: inferences of magma source and melt generation from olivine and its melt inclusions. PhD thesis in Earth Science, Universidad Complutense de Madrid – Université Clermont-Auvergne.
- Haskin, L.A., Wang, A., Rockow, K.M., Jolliff, B.L., Korotev, R.L., Viskupic, K.M. (1997) Raman spectroscopy for mineral identification and quantification for in situ planetary surface analysis: a point count method. *Journal of Geophysical Research* 102, 19293-19306.
- Lamadrid, H.M., Moore, L.R., Moncada, D., Rimstidt, J.D., Burruss, R.C., Bodnar, R.J. (2017) Reassessment of the Raman CO<sub>2</sub> densimeter. *Chemical Geology* 450, 210-222.
- Laporte, D., Hardiagon, M., Provost, A. (2016) Ascent and degassing of magmas: the conditions of homogeneous bubble nucleation in the system basalt-CO<sub>2</sub>. *EMPG XV-International Conference*, Zürich.
- Medjoubi, K., Leclercq, N., Langlois, F., Buteau, A., Lé, S., Poirier, S., Mercère, P., Sforza, M.C., Kewish, C.M., Somogyi, A. (2013) Development of fast, simultaneous and multi-technique scanning hard X-ray microscopy at Synchrotron Soleil. *Journal of synchrotron radiation* 20, 293-299.
- Somogyi, A., Medjoubi, K., Baranton, G., Le Roux, V., Ribbens, M., Polack, F., Philippot, P., Samama, J-P. (2015) Optical design and multi-length-scale scanning spectro-microscopy possibilities at the Nanoscopium beamline of Synchrotron Soleil. *Journal of synchrotron radiation* 22, 1118-1129.
- Tucker, J.M., Hauri, E.H., Pietruszka, A.J., Garcia, M.O., Marske, J.P., Trusdell, F.A. (2019) A high carbon content of the Hawaiian mantle from olivine-hosted melt inclusions. *Geochimica et Cosmochimica Acta* 254, 156-172.
- Venugopal, S., Schiavi, F., Moune, S., Bolfan-Casanova, N., Druitt, T., Williams-Jones, G. (2020) Melt inclusion vapour bubbles: the hidden reservoir for major and volatile elements. *Scientific Reports* 10, 9034, doi: 10.1038/s41598-020-65226-3.
- Wang, X., Chou, I.M., Hu, W., Burruss, R.C., Sun, Q., Song, Y. (2011) Raman spectroscopic measurements of CO<sub>2</sub> density: experimental calibration with high-pressure optical cell (HPOC) and fused silica capillary capsule (FSCC) with application to fluid inclusion observations. *Geochimica Cosmochimica Acta* 75, 4080–4093.
- Yesiltas, M., Jaret, S., Young, J., Wright, S.P., Glotch, T.D. (2018) Three-dimensional Raman tomographic microspectroscopy: a novel imaging technique. *Earth and Space Science* 5, 380-392.

